Inorganic Chemistry

ARTICLE

pubs.acs.org/IC

# Morphology-Controlled Synthesis of Hematite Nanocrystals and Their Facet Effects on Gas-Sensing Properties

Yong Yang,[†,‡] Haixia Ma,[*,†] Jing Zhuang,[‡] and Xun Wang[*,‡]

[†]College of Chemical Engineering, Northwest University, Xi'an 710069, P. R. China

[‡]Department of Chemistry, Tsinghua University, Beijing, 100084, P. R. China

Supporting Information

**ABSTRACT:** An oriented attachment growth process was found for the morphology and shape control of various inorganic materials in solution-based systems. In this Article, a well-defined iron oxide polyhedron was prepared via a simple hydrothermal method. Detailed investigations revealed that the single-crystalline polyhedron evolved from polycrystalline aggregates. The shape and size control of the iron oxide crystals were achieved by simply adjusting the synthesis parameters. The as-prepared products exhibit excellent gas sensing selectivity to ethanol vapor. The gas-sensing ability is closely related to the exposure of high-index facets.

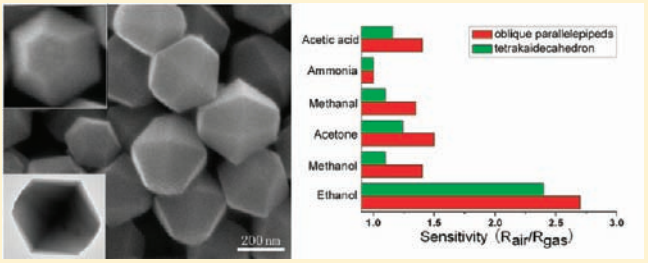


## INTRODUCTION

Morphological control over inorganic crystals has attracted intensive attention because of the promoted physical and chemical properties stemming from the different crystal facets.[1−4] A number of polyhedral-shaped crystals, including oxides and noble metals, have been reported.[5−9] Generally, various structures of different dimensions and shapes have been synthesized as a result of difference in growth rates along different crystallographic facets. However, the basic principle about nanostructures assembled from primary species to single crystals is still far from being well understood, especially for nanoparticles exposing high-index facets. A better understanding of the synthesis mechanism will benefit the preparation of nanostructures with those facets.

To date, the crystal growth has been usually explored based on two fundamental mechanisms: Ostwald ripening and Oriented attachment (OA). The former can be briefly described as the growth of larger crystals at the expense of smaller ones.[10,11] According to the Gibbs-Thompson equation and Fick's principle, the free energy increases with the decrease in particle size, which leads to the smaller ones becoming smaller and vanishing eventually.[12] However, crystal growth is a complex process and highly depends on solution, capping ligands, temperature, and interface between the particles. This mechanism seems to be unable to adequately describe the polycrystalline products with randomly oriented primary crystals.[13,14] Special morphologies and controllable sizes are all well-explained by oriented aggregation growth, in which a single crystal was formed by self-organization of adjacent particles in a common crystallographic structure.[15−20] More recently, we further found that the size and surface properties may determine the initial assembly of nuclei and the subsequent crystal growth process, and in quite diverse systems, the growth modes of nanocrystals can be tuned by changing their size and surface properties.[21] In this paper, OA took place under hydrothermal conditions, which was found to guide the growth of a well-defined iron oxide polyhedron. The formation mechanism involved the primary nanoparticle self-assembled into large aggregates and eventually recrystallized into a single crystalline polyhedron under high temperature conditions.

Hematite ($\alpha$-$Fe_2O_3$) as an environment-friendly material has been the subject of studies for a wide variety of potential applications,[22−25] and considerable efforts have been made in the synthesis of various morphologies.[26−33] Shape-controlled polyhedral crystals were usually achieved by means of introducing some ligands, such as surfactants or inorganic anions, into their reaction systems. Recently, Gao and co-workers have reported on the synthesis of unusual tetrakaidecahedral and oblique parallelepiped iron oxide bound by high-index facets with unusual magnetic properties, in which the corresponding growth mechanism is not discussed in detail.[34] Xu and Lv et al. have prepared a bipyramidal dodecahedral structure enclosed by (101) planes or an octodecahedral structure enclosed by (101) and (111) planes, by the adsorption of fluoride ions.[35] It is necessary to further explore the growth of the $\alpha$-$Fe_2O_3$ crystals for the synthesis of various morphologies to expand its application ranges.

In this Article, we report the synthesis of well-shaped polyhedral single-crystalline $\alpha$-$Fe_2O_3$ particles by the hydrothermal method. Selective adhesion of CMC on the facet alters the crystal habits significantly. The growth phenomenon may open a new way for controllable synthesis of crystals. At the same time, the

**Received:** May 24, 2011
**Published:** September 16, 2011

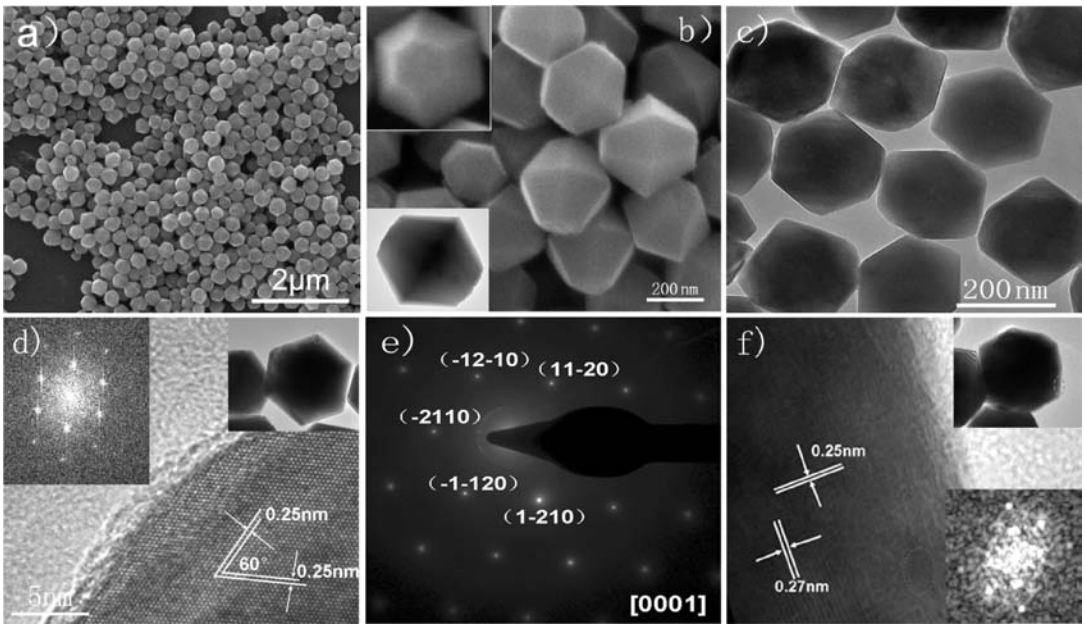


**Figure 1.** The tetrakaidecahedral $\alpha$-$Fe_2O_3$ nanocrystals synthesized at 200 °C for 6 h. (a,b) Low- and high-magnification SEM image of tetrakaidecahedral $\alpha$-$Fe_2O_3$ crystals. Insets (top left and bottom left) represents the cross-section of the as-prepared product and HRTEM images of a single tetrakaidecahedral crystal; (c) TEM image of the tetrakaidecahedral $\alpha$-$Fe_2O_3$ crystals; (d) HRTEM images and the corresponding fast Fourier-transform (FFT) pattern (top left). The insets (top right) are corresponding sites selected for analysis; (e) SEAD patterns from the [0001] zone axis; (f) HRTEM image of a representative $\alpha$-$Fe_2O_3$ nanoparticle and the corresponding FFT patterns (bottom). The insets (top right) are corresponding to sites selected for analysis.

effect of the reaction parameters on the final morphologies and sizes of iron oxide crystals are also investigated in detail. Correspondingly, the obtained samples exhibit outstanding gas-sensing performance over ethanol. The surface structure of the crystals has significant contribution to their gas-sensing response.

## EXPERIMENTAL SECTION

**Materials.** All chemicals were purchased from Beijing Chemical Reagent Company, including potassium ferrocyanide ($K_4Fe(CN)_6 \cdot 3H_2O$), carboxyl methyl cellulose (CMC), methyl cellulose (MC), poly(vinylpyrrolidone) (PVP, MW = 30 000), and hydrazine hydrate ($N_2H_4 \cdot H_2O \geq 50\%$) was purchased from Beijing Yili Fine Chemcial Co., Ltd/ The chemicals were of analytical grade and were used as received without further purification. Deionized water was used throughout the experiment.

**Preparation of $\alpha$-$Fe_2O_3$ Crystals.** The $\alpha$-$Fe_2O_3$ tetrakaidecahedra were prepared on a large scale by a hydrothermal method. In a typical procedure, a mixture of $K_4Fe(CN)_6 \cdot 3H_2O$ (0.6 mmol), 1.25 g $L^{-1}$ sodium carboxymethyl cellulose solution (CMC, 30 mL), PVP (400 mg), and $N_2H_4 \cdot H_2O$ solution (0.4 mL) were added successively into a 40 mL Teflon-lined autoclave under magnetic stirring at room temperature. The autoclave was heated and maintained at 200 °C for 6 h. After the reaction, the autoclave was allowed to cool to room temperature naturally. The red precipitate was collected from the supernatant solution by centrifugation and then washed with deionized water and ethanol several times.

The influences of the amount of $K_4Fe(CN)_6 \cdot 3H_2O$ and $N_2H_4 \cdot H_2O$ on the morphology of $\alpha$-$Fe_2O_3$ nanostructures were investigated. For the synthesis of oblique parallelepiped crystals, a mixture of $K_4Fe(CN)_6 \cdot 3H_2O$ (0.2 mmol), $N_2H_4$ solution (0.4 mL), PVP (400 mg), and 1.25 g $L^{-1}$ sodium carboxymethyl cellulose (30 mL) solution was kept at 200 °C under hydrothermal conditions for 6 h. The red product was collected by centrifugation. The amount of $K_4Fe(CN)_6$ decreases to 0.4 mmol maintaining a constant reaction condition to prepare the mixture of oblique parallelepipeds and tetrakaidecahedra. The polyhedral $\alpha$-$Fe_2O_3$ crystals with different sizes were obtained by adjusting the amounts of $N_2H_4 \cdot H_2O$. The same amount of $NH_3 \cdot H_2O$ was used to replace $N_2H_4 \cdot H_2O$ to investigate the role of $N_2H_4 \cdot H_2O$ in shape controlled synthesis of the nanocrystals.

**Characterization.** The phase structure of the products was determined by XRD on a Rigaku D/max-2400 X-ray diffractometer using CuK radiation ($\lambda$= 1.5418 Å) at 40 kV voltage and a 40 mA current ranging from 20° to 80°. The morphology and size of the nanostructures were determined by a FEI Sirion200 scanning electron microscope (SEM) at 10 kV, Hitachi H-7650B transmission electron microscope (TEM) at 80 kV, and a FEI Tecnai G2 F20 S-Twin high-resolution transmission electron microscope (HRTEM) at 200 kV. X-ray photoelectron spectroscopy (XPS) was performed on a PHI-5300 with an Al−Mg double anode target as the exciting source with 80KcPS angle distinguish and a resolution of 0.08 eV. The specific surface area of the sample was calculated from the results of $N_2$ physisorption following the multipoint Brunauer−Emmett−Teller (BET) procedure using a Quantachrome-1 sorption analyzer.

**Gas-Sensing Measurements.** The sensor structure and the testing method were similar to that of previous reports.[36] The gas-sensing properties were performed through a WS-60A testing system of gas sensors (Weisheng Instruments Co., Zhengzhou, China).[9] The gas sensors were fabricated by coating an aqueous slurry of the prepared products onto the ceramic tubes of the sensor body without an additional annealing process except for aging in the gas sensor system. Typically, the prepared gas sensor was placed in a shielded chamber; an alloy coil through the tube was employed as a heater to control the operating temperature; and the electrical contact was made through connecting the four platinum wires with the instrument base by silver paste. The gas sensing experiments were conducted under a pressure of 1 standard atmosphere (atm) and at relative humidity of 10−20%. The heating voltage is 0.55 V and the working temperature is about 350 °C, respectively. An appropriate amount of different gases or vapors such as ethanol, acetone, methanol, methanal, ammonia, and acetic acid


dx.doi.org/10.1021/ic201104w |*Inorg. Chem.* 2011, 50, 10143–10151

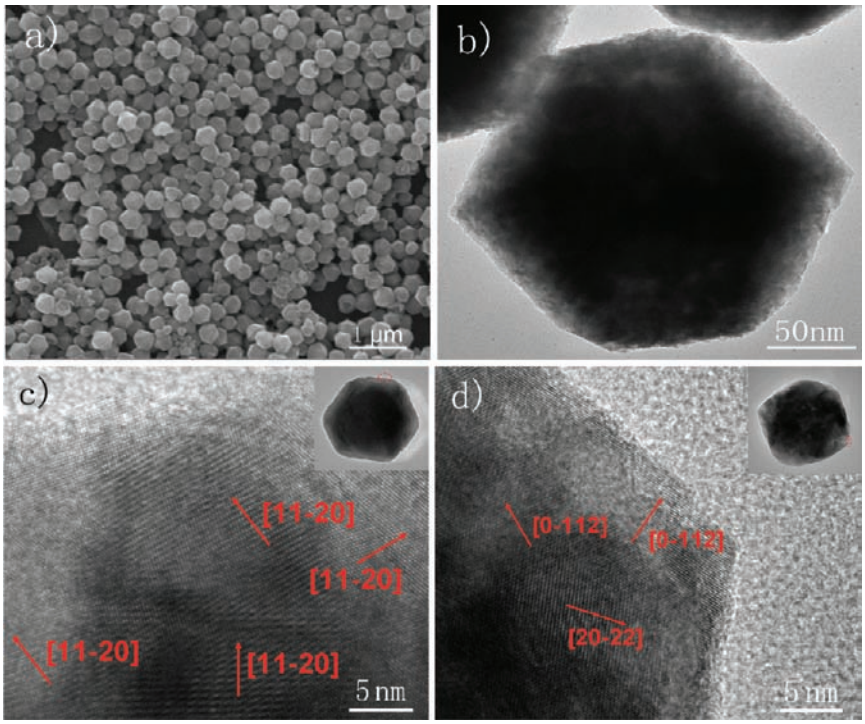


**Figure 2.** The tetrakaidecahedral $\alpha$-$Fe_2O_3$ single crystals synthesized at 160 °C for 6 h. (a) TEM image of the $\alpha$-$Fe_2O_3$ crystals; (b) TEM image of the tetrakaidecahedral $\alpha$-$Fe_2O_3$ crystals; (c,d) HRTEM analysis of the surface areas, which are composed of tiny grains with random misorientation. The insets are corresponding sites selected for analysis.

were introduced into the closed chamber by a microinjector, and the sensor was exposed to air again by opening the chamber. The sensitivity could be measured when the detecting gas was mixed with air homogeneously. Here, the gas sensitivity is defined as $R_a/R_g$, where $R_a$ and $R_g$ are the resistance of the sensor in clean air and in detected gas, respectively.

## RESULTS AND DISCUSSION

**Single Crystals of Polyhedral $\alpha$-$Fe_2O_3$.** Scanning electron microscope (SEM) images provide initially insight into the microstructure and morphology of the product. Figure 1a,b shows SEM images of typical polyhedral $\alpha$-$Fe_2O_3$ crystals synthesized at 200 °C for 6 h at different magnifications. The high-magnification SEM image given in Figure 1b shows that polyhedral crystals were well-shaped and scaled to around diameters of 200−250 nm and lengths of 300−350 nm. Highly symmetric feature can be clearly observed from the image of the cross-section of the as-prepared product (inset of Figure 1b). It is obvious to see that almost all of the particles are tetrakaidecahedral shape containing 2 top hexagon surfaces and 12 trapezoid side surfaces. Each polyhedron is composed of 14 facets and 30 edges. Figure 1c shows a typical TEM image of tetrakaidecahedral $\alpha$-$Fe_2O_3$ crystals. The fringes in a typical HRTEM image are separated by 0.25 nm at an angle of 60°, which agrees well with the (11−20) lattice spacing of the rhombohedral hematite (Figure 1d). The corresponding SAED pattern (Figure 1e) further confirms that the sample is single crystals with a perfect hexagonal spot pattern, which are attributed to (-2110), (-12-10), (11-20) planes under the incident electron beam along the [0001] direction. It indicates that two top surfaces are ascribed to (0001) and (000-1) planes, respectively. Similar results can be obtained from the FFT pattern shown in the inset of Figure 1d. On the first impression, the six surrounding planes of the tetrakaidecahedra are symmetric and they could be attributed to (11-20). However, Figure 1f shows two kinds of lattice fringes are identified when the crystals were laid-down to the background (inset of Figure 1f), and the typical lattice fringe spacing were determined to be 0.25 and 0.27 nm, which could be indexed to be the (-2110) and (01-1-4) planes, respectively. Similar results could be obtained from its FFT transformation (inset of Figure 1f). These results suggest that the crystals are enclosed by two symmetric (0001) and (000-1) planes as basal surfaces and (1-102), (1-10-2), (0-11-2), (0-112), (-101-2), (-1012), (-110-2), (-1102), (01-1-2), (01-12), (10-1-2), (10-12) as side surfaces. Some residual grain boundaries on the surfaces can be detected by the dashed line in Figure 1f. It indicates that these single crystals evolved from their polycrystalline forms. A geometrical model of an ideal tetrakaidecahedron enclosed by these crystal planes is put forward (Supporting Information Figure S1a), and it is in good accord with the as-synthesized tetrakaidecahedral crystals.

It is worth mentioning that polyhedral $\alpha$-$Fe_2O_3$ could be synthesized at 160 °C for 6 h. Figure 2a,b shows the product is composed predominantly of tetrakaidecahedron. However, there are still some uncompleted and broken octahedral crystals with a core−shell structure. The polycrystalline nature of these particles can be clearly detected from Figure 2c,d by the detection of some randomly oriented primary crystals, which indicates that they were not single crystals. It was further confirmed that they were formed through the self-assembly of tiny crystals into polycrystalline aggregates followed by recrystallization to single crystals under high temperature conditions. The recrystallization direction may take place from the core to the surface.

Ag nanocrystals with particle, wire, and cube shapes can be easily fabricated by tuning the concentration of precursors and


dx.doi.org/10.1021/ic201104w |*Inorg. Chem.* 2011, 50, 10143–10151

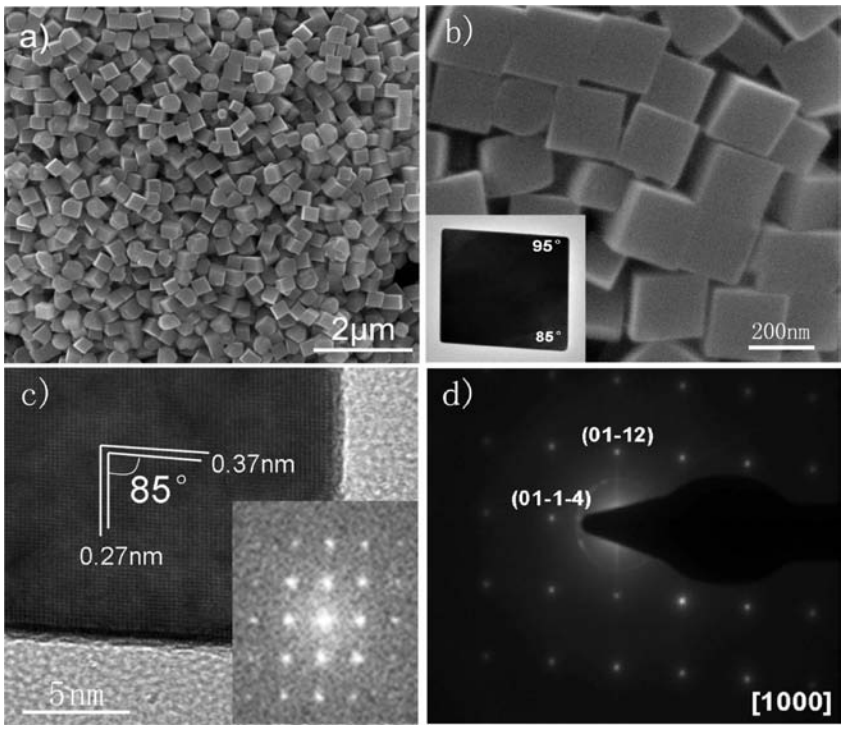


**Figure 3.** (a,b) Low- and high-magnification SEM image of oblique parallelepiped $\alpha$-$Fe_2O_3$ nanocrystals. HRTEM images of a single oblique parallelepiped nanocrystals (bottom left); (c) HRTEM images and the corresponding fast Fourier-transform (FFT) pattern (inset); (d) SEAD patterns from the [0001] zone axis.

the molar ratio between poly(vinylpyrrolidone) (PVP) and precursors in the polyol process.[7] In order to investigate the influence of the concentration of precursors, the amount of $K_4Fe(CN)_6$ was decreased to 0.2 mmol when keeping a constant reaction temperature. The morphology of the product varied from tetrakaidecahedra to oblique parallelepipeds. Figure 3a,b shows SEM images of typical oblique parallelepiped crystals at different magnifications. More than 90% of the crystals are well-shaped cubelike. Some of the surfaces of crystals seem to be rough (Figure 3a), and the possible reason is ascribed to the secondary growth of crystals. The sample has a cubelike morphology with an average edge length of 250 nm (Figure 3b). HRTEM image (inset of Figure 3b) shows that the angles between the edges at the corners of the particles can be divided into two styles: 95° and 85°. Two sets of clear lattice fringes with the interplanar distance of 0.27 and 0.37 nm at an angle of 85° (Figure 3c), which can be indexed to the (01-1-4) and (01-12) planes of rhombohedral $\alpha$-$Fe_2O_3$ structure, respectively. Excellent crystallinity is also confirmed by corresponding SEAD patterns (Figure 3d). Similar results could be obtained from its FFT transformation (inset in Figure 3c). This structure is in good agreement with the data from Gao et al.[34] From the above characterizations, we can conclude that the crystals are single crystals bound by (01-12), (01-1-4), and (-2110) planes. Figure S1b in the Supporting Information presents a geometrical model of the as-prepared oblique parallelepiped enclosed by those facets.

It has been found experimentally that the final product morphology of polyhedral $\alpha$-$Fe_2O_3$ crystals strongly depends on the concentration of precursor. When the amount of $K_4Fe(CN)_6$ decreases to 0.4 mmol, a constant reaction temperature is maintained at 200 °C. The morphology of the product varied gradually from tetrakaidecahedra to the mixture of oblique parallelepipeds and tetrakaidecahedra (Supporting Information, Figure S2). Further characterizations were performed to learn their phase and composition. Both the samples (Figure S3 in the Supporting Information) are well indexed to the standard data of pure rhombohedral $\alpha$-$Fe_2O_3$ [space group, $R3\bar{c}$ (167)] (JCPDS card 33-0664). In additional, the wide-survey XPS spectrum (Figure 4a) of the as-prepared sample reveals the predominant presence of carbon, oxygen, and iron. Figure 4b shows the Fe2p XPS spectrum of the composites. The 2p photoelectron peaks appear near 719 eV and are characteristic of $Fe^{3+}$ in $Fe_2O_3$. The binding energies of Fe2p are consistent with the previously reported values for the bulk $Fe_2O_3$.[37] Thus, the Fe2p and O1s spectra indicate that the valence states of elements Fe and O are +3 and −2, respectively. No component related to zerovalent Fe and/or $Fe^{2+}$ is observed, and it indicates high purity of the samples.

**Growth Mechanism.** Time-dependent experiments were carried out to disclose the formation mechanism of the polyhedral $\alpha$-$Fe_2O_3$ crystals in detail. Figure 5 shows SEM images of the products synthesized at different reaction times. It can be seen that the $\alpha$-$Fe_2O_3$ crystals undergo an evolution from tiny nanoparticles to polyhedrons. When the reaction time was as short as 0.5 h, the product exhibits irregular-nanostructure with a diameter of about 100 nm. These $\alpha$-$Fe_2O_3$ crystals are composed of numerous tiny particles (inset of Figure 5a). Driven by the reduction in surface energy, the crystal nucleus tends to assemble from primary species to eliminate the interfaces under hydrothermal conditions. With an increase of the reaction time to 1 h (Figure 5b), the irregular-nanostructure transforms to a sphere-shape with a continuously enlarged size. As time elongated to 3 h, it is notable that the products are composed predominantly of polyhedron (Figure 5c) with a rough surface, which indicates that

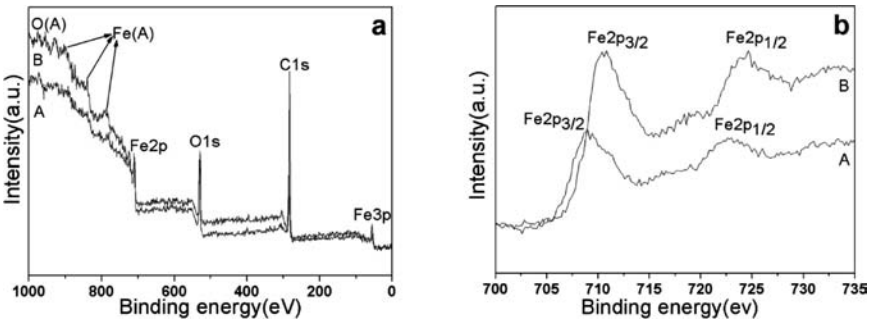


**Figure 4.** (a) XPS spectrum of the composites; (b) Fe2p XPS spectrum (A, tetrakaidecahedral iron oxide crystals; B, oblique parallelepiped iron oxide crystals).

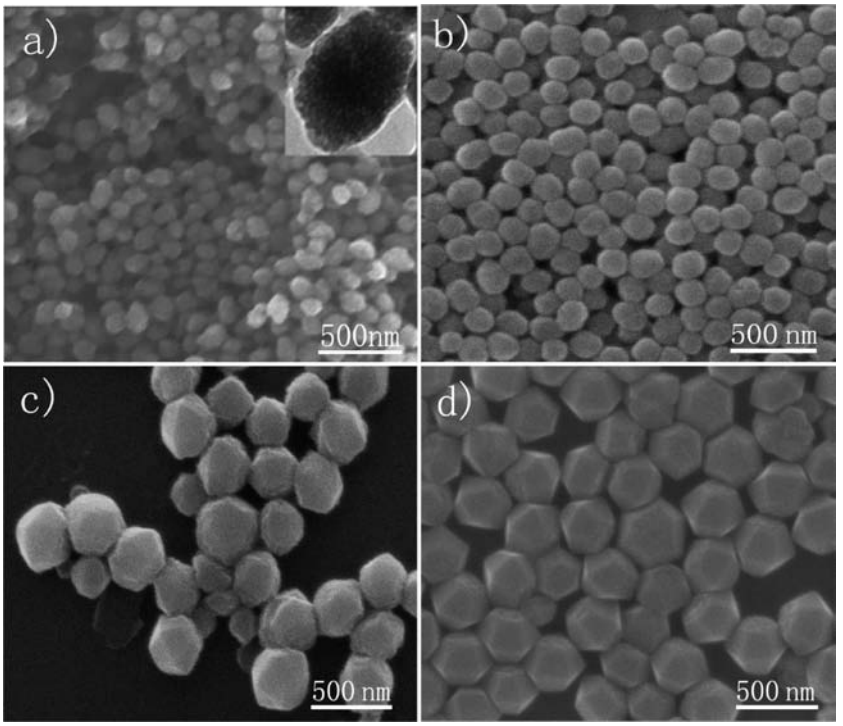


**Figure 5.** SEM images of the as-prepared products at 200 °C at different reaction times: (a) 0.5, (b) 1, (c) 3, and (d) 6 h.

recrystallization is still underway. After the reaction was further prolonged to 6 h (Figure 5d), the morphology was not changed but smooth surfaces of the nanocrystal were obtained. The size and morphology of the product remained the same even at longer reaction time. As previously studied, an aggregation of solid material was followed by surface crystallization, which is a further coarsening process of the particles after their assembly, resulting in smooth surfaces.[38,39] On the basis of these results, the formation mechanism of well-shaped $\alpha$-$Fe_2O_3$ crystals could be summarized as follows: Initially, $[Fe(CN)_6]^{4-}$ ions dissociate slowly into $Fe^{2+}$ ions. Then, the $Fe^{2+}$ ions are subsequently oxidized in aqueous solution to form FeOOH or $Fe(OH)_3$. Finally, the $\alpha$-$Fe_2O_3$ crystals could form through the hydrolytic process. The growth mechanism does not follow the classic crystal growth route, i.e., the formation of the single crystal was obtained by the original nucleus and extends further outward. It is rational to conclude that the single crystalline polyhedron crystals structure was obtained from polycrystals to single crystals after nucleation. To clearly demonstrate the formation of the $\alpha$-$Fe_2O_3$ single crystal, a nucleation-assembly recrystallization (NAR) mechanism is given in Scheme 1.

**Influences of Reaction Parameters.** It is known that the macromolecules absorbed on the surface of nanoparticles have a great influence on their self-assembly behavior. In our synthesis process, both the additions of macromolecules CMC and PVP are the key factors to form polyhedral structures. As is known to all, CMC contains many carboxymethyl side groups and is commonly used as a stabilizer and thickener. A series of experiments were carried out to clarify the effect of surfactant on the morphology. Controlled experiments showed that only a microdendritic structure (Figure S4a in the Supporting information) was obtained without CMC under the same reaction conditions. The dendritic structure was formed as a result of fast growth along six equivalent directions.[40,41] It has been well acknowledged that carboxylic anions have a strong chelating ability to transition metal ions.[42] According to the literature,[43] the (0001) plane of $\alpha$-$Fe_2O_3$ includes doubly coordinated surface hydroxyl groups whereas singly coordinated surface hydroxyl groups are

**Scheme 1. Schematic Illustration of the Formation Mechanism of $\alpha$-$Fe_2O_3$ Single Crystal in the Synthetic Process**

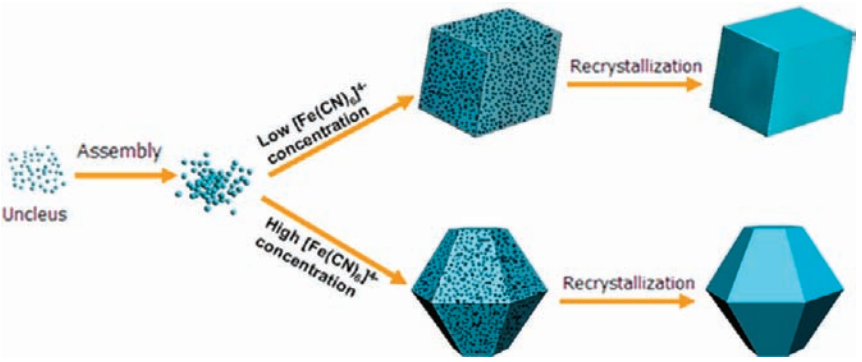


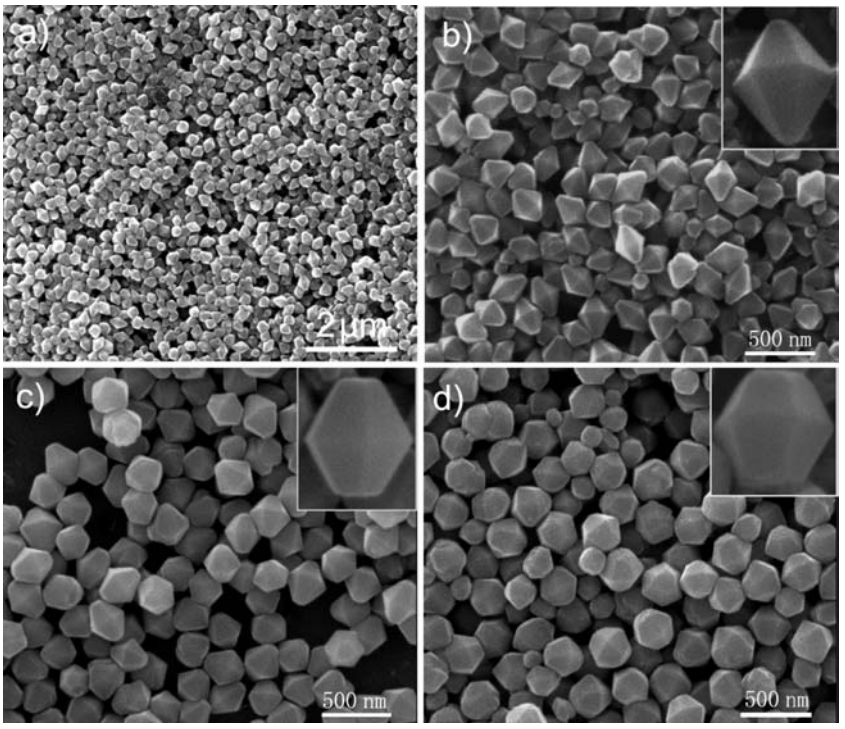


**Figure 6.** SEM images of $\alpha$-$Fe_2O_3$ products prepared with different concentrations of CMC: (a,b) 0.25, (c) 0.75, and (d) 1.25 g $L^{-1}$.

present on other planes. The presence of viscous CMC solution, which may be selectively adsorbed on some facets of the crystal, will adjust the growth rates and result in anisotropic growth of a polyhedral structure For instance, with the increase of the concentration of the CMC solution from 0.25 to 1.25 g $L^{-1}$ (Figure 6) while other conditions are kept constant, the different aspect ratio tetrakaidecahedral $\alpha$-$Fe_2O_3$ crystals can be obtained. A high concentration of CMC solution may have more affinity on the (0001) plane and confines the growth of hematite crystals along the [0001] direction. Therefore, the different aspect ratio polyhedron can be derived from the specific adsorption of carboxymethyl side groups on the crystal planes, which restrains the crystal growth perpendicular to the *c*-axis. As the concentration of CMC solution increases to 4 g $L^{-1}$, the final morphology gradually became monoplanes (Figure S5 in the Supporting information). Carboxymethyl side groups play an importance role in forming anisotropic growth of a polyhedral structure. The results further confirmed that the flowerlike structure (Figure S6 in the Supporting Information) was obtained with the addition of methyl cellulose (MC).

The surfactant PVP was found to be widely used as a protective agent to prevent nanoparticles from aggregation in the chemical preparation of crystals. The $\alpha$-$Fe_2O_3$ particles obtained in the absence of PVP are still tetrakaidecahedral (Figure S7 in the Supporting Information). The quality of polyhedral $\alpha$-$Fe_2O_3$ crystals would be greatly improved with the help of PVP. It was found that PVP surfactant contributed not only to dispersing the $\alpha$-$Fe_2O_3$ crystals but also to controlling the assembly rate, thus favoring uniform formation of the final morphology. These results indicate that the well-shaped polyhedral $\alpha$-$Fe_2O_3$ crystals result from the coordinative effect of CMC and PVP.

In neutral solution, the ionization of $[Fe(CN)_6]^{4-}$ is weak. However, in the presence of $N_2H_4 \cdot H_2O$, the ionization of


dx.doi.org/10.1021/ic201104w |*Inorg. Chem.* 2011, 50, 10143–10151

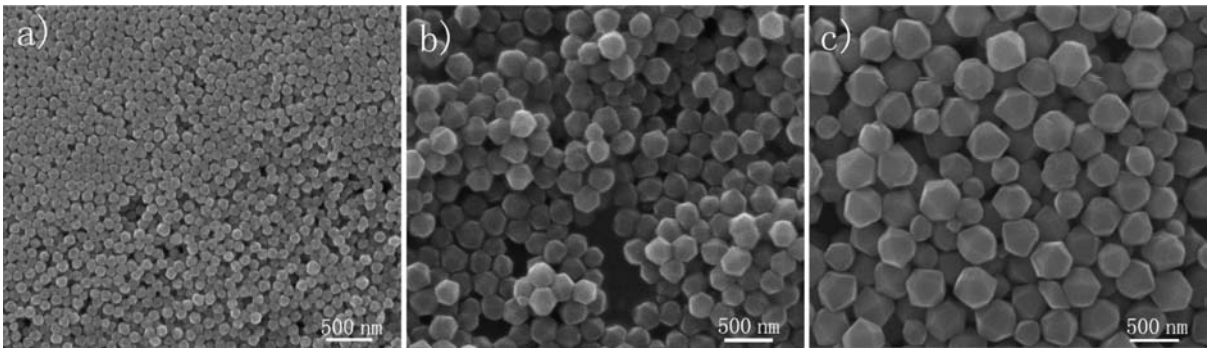


**Figure 7.** SEM images of the samples prepared with a different amount of $N_2H_4$ solution: (a) 0.2, (b) 0.4, and (c) 0.6 mL.

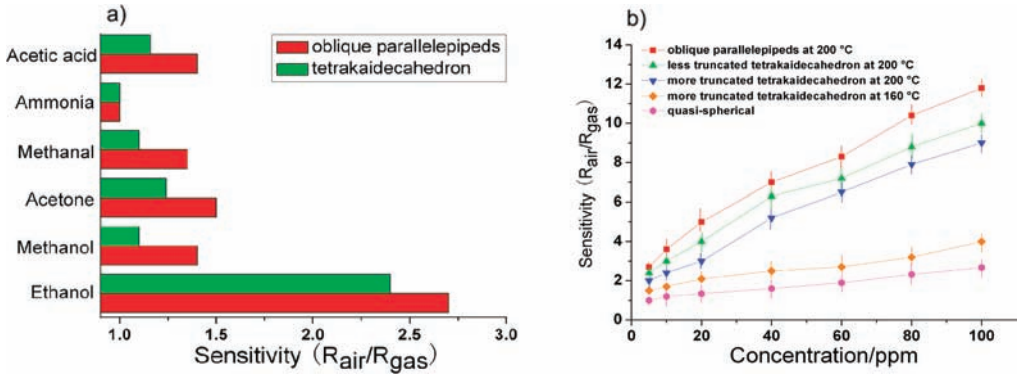


**Figure 8.** (a) Sensitivity of the sensors based on as-prepared $\alpha$-$Fe_2O_3$ toward different gases or vapors at a concentration of 5 ppm. (b) Sensitivity curves of $\alpha$-$Fe_2O_3$ particles with different shapes as a function of ethanol concentration.

$[Fe(CN)_6]^{4-}$ will accelerate.[44] Controlled experiments indicate that spherical particles were synthesized when $N_2H_4 \cdot H_2O$ was not involved in the experiment under the same reaction conditions (Figure S4b in the Supporting Information). In addition, only spherical particles with an average diameter of 200 nm can be obtained in the presence of $NH_3 \cdot H_2O$ rather than $N_2H_4 \cdot H_2O$ (Figure S8 in the Supporting Information). The result show that $N_2H_4 \cdot H_2O$ can kinetically manipulate the growth rate of crystals, resulting in the anisotropic growth of the crystals. If other simple iron precursors, such as $FeCl_3$, $Fe(NO_3)_3$, and $Fe_2(SO_4)_3$, are treated under the same hydrothermal conditions, the $\alpha$-$Fe_2O_3$ particles obtained were not polyhedral. Formation of a polyhedron needs a suitable iron complex precursor that slowly dissociates to yield $Fe^{2+}$ ions. A higher dose of $N_2H_4 \cdot H_2O$ will result in increased alkalinity, which could speed up the ionization of $[Fe(CN)_6]^{4-}$. The size of the final products gradually increased with the increase of $N_2H_4 \cdot H_2O$ while other conditions were constant (Figure 7). The size of the polyhedral $\alpha$-$Fe_2O_3$ crystals could be tailored in such a way.

**Gas Sensors Performance.** Semiconductor crystals have been of great interest for their applications in a variety of fields due to their unique properties. $\alpha$-$Fe_2O_3$ belongs to the n-type semiconductors and is usually used as a gas sensing material. It has been reported by many researchers that the $\alpha$-$Fe_2O_3$ sensor exhibits an excellent gas-sensing property to some combustible or toxic gases.[45,46] The gas sensing properties are directly related to its preparation method, size, aspect ratio, and crystalline degree. The as-prepared samples are found to be bound by high-index facets; those surface properties differ from other common planes. Encouraged by this, it is rational that the obtained polyhedral $\alpha$-$Fe_2O_3$ crystals should show good performance in a gas sensor.

Figure 8a shows the gas-sensing measurement of the two kinds of as-prepared $\alpha$-$Fe_2O_3$ nanostructures in response to a variety of inflammable and corrosive gases such as ethanol, acetone, methanol, methanal, ammonia, and acetic acid. Our results showed that the sensitivity of the obtained sensor to ethanol atmosphere was higher than other gases and was barely sensitive to ammonia at a low concentration. The possible reason is the weak redox capability of ammonia and the weak chemical interaction between ammonia and the surface of $\alpha$-$Fe_2O_3$.

We selected $\alpha$-$Fe_2O_3$ nanoparticles (about 300 nm in diameter, Figure S7 in the Supporting Information) as reference to evaluate the gas sensor performance of as-prepared samples. The corresponding gas-sensing curves comparison of the five types of $\alpha$-$Fe_2O_3$ nanostructure was the plot of the gas sensitivity versus $C_2H_5OH$ concentration shown in Figure 8b. It can be seen that the response of the sensor based on the polyhedral $\alpha$-$Fe_2O_3$ synthesized at 200 °C increased dramatically with the increase in the ethanol vapor concentration and was much higher than that of the reference under the same ethanol concentration. It is obvious that the sensitivity of the sensor follows the sequence oblique parallelepipeds > less truncated degree polyhedral > more truncated degree polyhedral > quasi-spherical structure under a given $C_2H_5OH$ concentration. We also compared the tetrakaidecahedral $\alpha$-$Fe_2O_3$ synthesized at 200 and 160 °C, respectively. The response of the polyhedral $\alpha$-$Fe_2O_3$ synthesized at 200 °C is much higher than that of at 160 °C. That is to say, the gas-sensing ability is not only related to the exposure of high-index facets but also to their crystalline degrees.


dx.doi.org/10.1021/ic201104w |*Inorg. Chem.* 2011, 50, 10143–10151

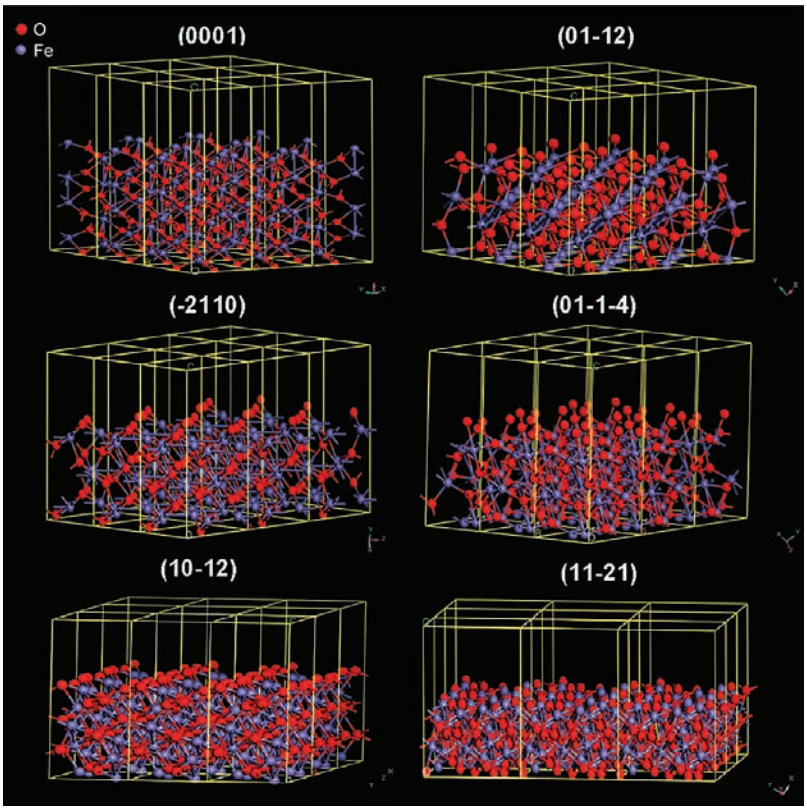


**Figure 9.** Crystal structures of different planes of $\alpha$-$Fe_2O_3$.

In order to illustrate the superior gas sensing property of the as-prepared $\alpha$-$Fe_2O_3$ crystals, the Brunauer−Emmett−Teller (BET) specific surface areas of oblique parallelepiped and tetrakaidecahedral crystals were carried out. The specific surface area was evaluated to be 8.892 and 5.043 $m^2\ g^{-1}$, respectively. This result indicates that the superior gas-sensing performance is not ascribed to the surface area but to the nature of the surface structure, which is closely correlated with the surface enclosed by high-index planes.

The change in resistance of semiconducting oxide gas sensors is primarily caused by absorption/desorption phenomena and reactions at the surface of the metal oxide. When the sensor is in air, the surface of $\alpha$-$Fe_2O_3$ is covered by plenty of oxygen adsorbents, such as $O^{2-}$, $O^-$, and $O_2^-$. The formation of the oxygen adsorbate layer leads to a decrease in the electron density on the sensor surface. Once the sensor is exposed to reducing molecules (here ethanol), ethanol molecules are oxidized by surface-adsorbed ionized oxygen species,[47] which results in the release of free electrons to the sensor, thus decreasing the potential barrier. As for the hematite crystal structure, a hematite crystal has a rhombohedrally centered hexagonal structure. Fe atoms are 6-fold-coordinated by O atoms. Also, the adsorption of oxygen species is closely related to structural defects on the surface, especially oxygen vacancies. Fe atoms are coordinatively unsaturated and may act as the active species for the gas reaction. From this consideration, the density of the exposed $Fe^{3+}$ cations on several high-index planes of the $\alpha$-$Fe_2O_3$ (Figure 9) crystal was calculated and the corresponding data were collected (Table S1 in the Supporting Information). The most common (11-21) plane of the corundum structure was selected for comparison. The density of exposed $Fe^{3+}$ cations in exposing facets is higher than that of the (11-21) plane. The highest density of the exposed $Fe^{3+}$ cations benefit the reaction of $C_2H_5OH$ and may provide active sites and facilitate the reaction to adsorption of organic molecules. We also compared the gas sensing performance of the different aspect ratio polyhedron. The gas sensing performance of the less truncated polyhedral was always better than that of the more truncated polyhedral. On the basis of the fact that it has a favorable gas-sensing property, the as-prepared $\alpha$-$Fe_2O_3$ nanostructure would be a promising candidate for a practical alcohol sensor.

## CONCLUSIONS

In summary, we reported a simple hydrothermal method to synthesize well-defined $\alpha$-$Fe_2O_3$ crystals. The NAR mechanism reveals that the transformation of $\alpha$-$Fe_2O_3$ crystals from polycrystals to single crystals after nucleation. In the presence of surfactant, CMC is selectively adsorbed on facets of the crystal, which will lead to anisotropic growth of a polyhedral structure. Moreover, the gas sensing behavior investigation shows that polyhedral $\alpha$-$Fe_2O_3$ crystals exhibit a good response to ethanol vapor. The enhancement of gas-sensing performance is attributed to the exposure of high-index facets. The present study not only provides an opportunity to acquire the knowledge of crystal growth and motivates us to synthesize other polyhedral metal oxide but also is an ideal candidate as a building block for studying their applications in advanced functional materials.

## ASSOCIATED CONTENT

**Supporting Information.** Geometrical model, XRD patterns, and TEM images of the hematite nanocrystals. This material is available free of charge via the Internet at http://pubs.acs.org.

## AUTHOR INFORMATION

**Corresponding Author**
*E-mail: wangxun@mail.tsinghua.edu.cn; mahx@nwu.edu.cn.

## ACKNOWLEDGMENT

This work was supported by NSFC (Grants 20725102 and 20921001) and the State Key Project of Fundamental Research for Nanoscience and Nanotechnology (Grant 2011CB932402).

## REFERENCES

(1) Yang, H. G.; Sun, C. H.; Qiao, S. Z.; Jin, Z.; Liu, G.; Smith, S. C.; Cheng, H. M.; Lu, G. Q. *Nature* **2008**, *53*, 638.
(2) Tian, N.; Zhou, S.; Sun, S.; Ding, Y.; Wang, Z. L. *Science* **2008**, *316*, 732.
(3) Wang, X.; Zhuang, J.; Peng, Q.; Li, Y. D. *Nature* **2005**, *437*, 121.
(4) Kim, C.; Lee, H. *Catal. Commun.* **2009**, *10*, 1305.
(5) Lu, C. L.; Prasad, K. S.; Wu, H. L.; Ho, J. A.; Huang, M. H. *J. Am. Chem. Soc.* **2010**, *132*, 14546.
(6) Ma, Y. Y.; Kuang, Q.; Jiang, Z. Y.; Xie, Z. X.; Huang, R. B.; Zheng, L. S. *Angew.Chem., Int. Ed.* **2008**, *47*, 8901.
(7) Sun, Y. G.; Xia, Y. N. *Science* **2002**, *298*, 2176.
(8) Tao, A.; Sinsermsuksakul, P.; Yang, P. D. *Angew.Chem., Int. Ed.* **2006**, *45*, 4597.
(9) Han, X. G.; Jin, M. S.; Xie, S. F.; Kuang, Q.; Jiang, Z. Y.; Jiang, Y. Q.; Xie, Z. X.; Zheng, L. S. *Angew.Chem., Int. Ed.* **2009**, *121*, 9344.
(10) Ostwald, W. Z. *Phys. Chem.* **1900**, *34*, 495.
(11) Lifshitz, I. M.; Slyozov, V. V. J. *Phys. Chem. Solids.* **1961**, *19*, 35–50.
(12) Sugimoto, T. *Adv. Colloid Interface Sci.* **1987**, *28*, 65.
(13) Pradhan, N.; Efrima, S. *J. Phys. Chem. B.* **2004**, *108*, 11964.
(14) Nguyen, T. D.; Mrabet, D.; Do, T. O. *J. Phys. Chem. C.* **2008**, *112*, 15226.
(15) Pacholski, C.; Kornowski, A.; Weller, H. *Angew.Chem., Int. Ed.* **2002**, *41*, 1188.
(16) Halder, A.; Ravishankar, N. *Adv. Mater.* **2007**, *19*, 1854.
(17) Yu, J. H.; Joo, J.; Park, H. M.; Baik, S.-I.; Kim, Y. W.; Kim, S. C. *J. Am. Chem. Soc.* **2005**, *127*, 5662.
(18) Penn, R. L.; Banfield, J. F. *Scienc* **1998**, *281*, 969.
(19) Dirksen, J. A.; Ring, T. A. *Chem. Eng. Sci.* **1991**, *46*, 2389.
(20) Colfen, H.; Mann, S. *Angew. Chem., Int. Ed.* **2003**, *42*, 2350.
(21) Shen, S. L.; Wang, X. *Chem. Commun.* **2010**, *46*, 6891.
(22) Tsodikov, M. V.; Rostovshchikova, T. N.; Smirnov, V. V.; Kiseleva, O. I.; Maksimov, Y. V.; Suzdalev, I. P.; Ikorskii, V. N. *Catal. Today.* **2005**, *105*, 634.
(23) Chen, J. S.; Zhu, T.; Yang, X. H.; Yang, H. G.; Lou, X. W. *J. Am. Chem. Soc.* **2010**, *132*, 13162.
(24) Zhong, L. S.; Hu, J. S.; Liang, H. P.; Cao, A. M.; Song, W. G.; Wan, L. J. *Adv. Mater.* **2006**, *18*, 2426.
(25) Wu, P. C.; Wang, W. S.; Huang, Y. T.; Sheu, H. S.; Lo, Y. W.; Tsai, T. L.; Shieh, D. B.; Yeh, C. S. *Chem.—Eur. J.* **2007**, *13*, 3878.
(26) Gou, X. L.; Wang, G. X.; Park, J. S.; Liu, H.; Yang, J. *Nanotechnology* **2008**, *19*, 125606.
(27) Gou, X. L.; Wang, G. X.; Kong, X. Y.; Wexler, D; Horvat, J.; Yang, J.; Park, J. S. *Chem.—Eur. J.* **2008**, *14*, 5996.
(28) Wen, X. G.; Wang, S. H.; Ding, Y.; Wang, Z. L.; Yang, S. H. *J. Phys. Chem. B* . **2005**, *109*, 215.
(29) Jia, C. J.; Sun, L. D.; Luo, F.; Han, X. D.; Laura, J. H.; Yan, Z, G.; Yan, C. H.; Zheng, K. *J. Am. Chem. Soc.* **2008**, *130*, 16968.
(30) Cha, H. G.; Song, J. U.; Kim, H. S.; Shin, W. S.; Yoon, K. B.; Kang, Y. S. *Chem. Commun.* **2011**, *47*, 2441.
(31) Pan, Q. T.; Huang, K.; Ni, S. B.; Yang, F.; Lin, S. M.; He, D. Y. J. *Phys. D: Appl. Phys.* **2009**, *42*, 015417.
(32) Zhong, L. S.; Hu, J. S.; Liang, H. P.; Cao, A. M.; Song, W. G.; Wan, L. J. *Adv. Mater.* **2006**, *18*, 2426.
(33) Meng, L.; Chen, W. M.; Chen, C. P.; Zhou, H. P.; Peng, Q.; Li, Y. D. *Cryst. Growth Des.* **2010**, *10*, 479.
(34) Yin, J. Z.; Yu, Z. N.; Gao, F.; Wang, J. J.; Pang, H.; Lu, Q. Y. *Angew.Chem., Int. Ed.* **2010**, *49*, 6328.
(35) Lv, B. L.; Liu, Z. Y.; Tian, H.; Xu, Y.; Wu, D.; Sun, Y. H. *Adv. Funct. Mater.* **2010**, *20*, 3987.
(36) Zhang, J. T.; Liu, J. F.; Peng, Q.; Wang, X.; Li, Y. D. *Chem . Mater.* **2006**, *18*, 867.
(37) Mcintyre, N. S.; Zetaruk, D. G. *Anal. Chem.* **1977**, *49*, 1521.
(38) Xiang, G. L.; Zhuang, J.; Wang, X. *Inorg. Chem.* **2009**, *48*, 10222.
(39) Lipowsky, P.; Bowick, M. J.; Meinke, J. H.; Nelson, D. R.; Bausch, A. R. *Nat. Mater.* **2005**, *4*, 407.
(40) Cao, M. H.; Liu, T. F.; Gao, S.; Sun, G. B.; Wu, X. L.; Hu, C. W.; Wang, Z. L. *Angew.Chem., Int. Ed.* **2005**, *44*, 4197.
(41) Liang, J.; Li, L.; Song, W. M.; Fang, J. Z.; Luo, M.; Li, Y .P. *Cryst. Res. Technol.* **2010**, *45*, 405.
(42) Chen, L. Q.; Yang, X. F.; Chen, J.; Liu, J.; Wu, H.; Zhan, H. Q.; Liang, C. L.; Wu, M. M. *Inorg. Chem.* **2010**, *49*, 8411.
(43) Barron, V.; Torrent, J. J. *Colloid Interface Sci.* **1996**, *177*, 407.
(44) Zhao, L. J.; Duan, L. F. *Eur. J. Inorg. Chem.* **2010**, *36*, 5635–5639.
(45) Mao, D.; Yao, J. X.; Lai, X. Y.; Yang, M.; Du, J.; Wang, D. *Small.* **2011**, *7*, 578.
(46) Song, K.; Wang, Q.; Liu, Q.; Zhang, H. Q.; Cheng, Y. G. *Sensors* **2011**, *11*, 485.
(47) Kinkawa, T.; Sakai, G.; Tamaki, J.; Miura, N.; Yamazoe, N. J. *Mol. Catal. A* **2000**, *155*, 193.